

# High-Strength Steel Welding Research

*by*

*S. S. Babu, S. A. David, and G. R. Edwards<sup>†</sup>*

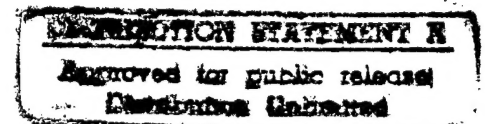
Oak Ridge National Laboratory, Oak Ridge, TN 37831 - 6096

<sup>†</sup>Colorado School of Mines, Golden, Colorado 80401

Report to

Office of Naval Research  
800 N. Quincy Street  
Arlington, VA 22217-5000

(May, 1997)



19970509 016

DTIC QUALITY INSPECTED 1

## Overview

This report is a summary of research performed at the Oak Ridge National Laboratory (ORNL) related to the high-strength steel welding project from November 1995 to December 1996. The overall Office of Naval Research Project aims at developing a low-cost welding consumable for high strength, high-toughness steel welds. In addition, more demanding requirements include that these welds must exhibit consistent properties over a wide range of welding condition and must be resistant to hydrogen cracking. These specifications require research on various aspects of microstructural development and its relation to the properties. In this project, the research tasks of the ORNL team are as follows:

1. Design of prototype welding consumable: The ORNL team will develop a thermodynamic model to predict the inclusion characteristics as a function of temperature for various consumable compositions.
2. Validation of the computer model: The inclusions in the prototype welds will be characterized by transmission electron microscopy. The results will be used to evaluate the predictive model developed in Task 1.

As a part of the Task 1, a phenomenological inclusion model was developed that is capable of predicting the inclusion characteristics, such as the sequence of oxide formation, inclusion composition, number density, and size, as functions of weld-metal composition and weld-metal cooling rate. In the previous report [1], the methodologies of the model and the results of the calculations on experimental weld compositions were described.

The research reported here constitutes the application of the modified inclusion model [2,3] and the results of Task 2. First, the cooling rate calculations were modified by using enhanced thermal conductivity values. Later on, the inclusion model was extended to consider the solidification effects with modified Clyne and Kurz equations [4,5]. Three experimental welds were chosen for detailed characterization based on the toughness results provided by Colorado School of Mines (CSM) [6]. The inclusion characteristics were evaluated in these welds and the experimental data were compared with the predictions of the model. The microstructures of experimental welds were characterized with optical and transmission electron microscopy. The observed microstructure development was analyzed with calculated continuous cooling transformation diagrams.

## 1. Introduction

Since the properties of the high-strength steel welds depend on the microstructure, it is necessary to understand important variables that control the weld microstructural development. It is known that, in addition to weld metal hardenability and weld cooling rate, the inclusion characteristics influence the microstructural development. Therefore, the research at ORNL focused on the development of a predictive model for inclusion formation and characterization of selected experimental welds. A series of experimental welds was produced by Lincoln Electric Company. These welds were produced at the same heat input levels to study the effect of inclusion formation and of the change in weld metal hardenability on the microstructure and properties. Three sets of welds, with increasing nickel concentrations, were produced at three base manganese concentrations as follows: (a) JR1267, JR1243, JR1273 (1 wt.% Mn base); (b) JR1274, JR1242, JR1279 (1.25 wt.% Mn base); and (c) JR1278, JR1279, JR1268 (1.5 wt.% Mn base). The experimental welds produced at 1 wt.% manganese base level were selected for evaluation at ORNL.

The charpy toughness properties of these welds were evaluated CSM. The charpy transition curves of the three welds are shown in Fig. 1 [6]. In general, the addition of nickel to welds has been shown to improve the toughness.

The mechanism for such a change in the toughness needs to be understood. Since the welding conditions were similar, the observed properties may be related to the effect of inclusions and/or of the weld metal hardenability on the microstructural development. This possibility necessitates detailed analysis of inclusions and of the microstructures of these three welds. A modified inclusion model was used to predict the inclusion characteristics.

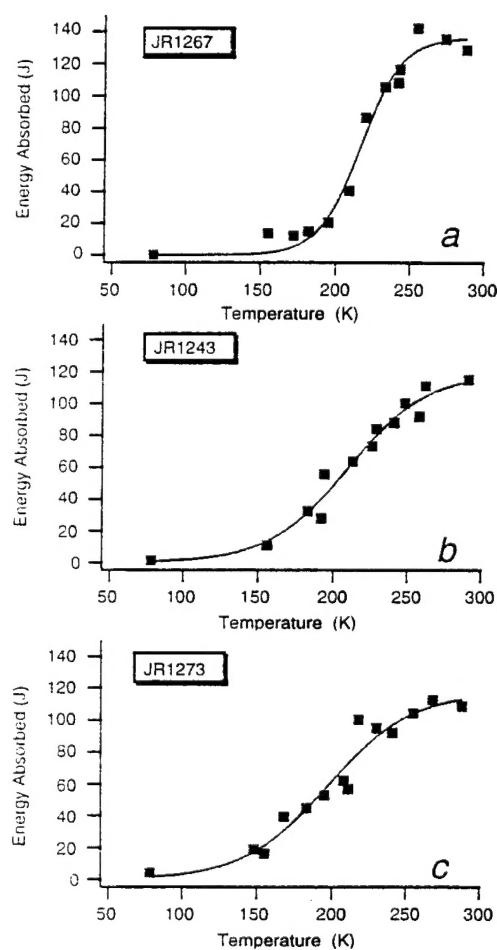


Fig. 1. Comparison of charpy toughness variation for three welds. The compositions are (a) 2 wt. % Ni, (b) 2.5 wt. % Ni and (c) 3 wt. % Ni. The solid lines are the best-fit curves confirming to a sigmoidal curve.

## 2. Modified Inclusion Model

The methodology of the inclusion model was discussed in the previous report [1]. However, the complexity of the solidification-induced sulfide and oxide formation was ignored. In this work, inclusion formation is described in two stages: (1) the oxide inclusion formation in the liquid steel in the temperature range of 2300 to 1800 K and (2) formation during solidification. In the first stage, the nucleation and growth of oxides are considered with an overall oxidation kinetic model; and in the later stages, the sulfide and complex oxide formation on pre-existing inclusions is considered. The multi-component partitioning and sulfide formation are treated with ThermoCalc™ software [7], using a published method described later [2,3]. The steps involved in the inclusion calculations are shown in a flow chart given in Fig. 2.

### 2.1 Inclusion Formation in the Liquid Steel

From the previous report, it is known that the inclusion model calculations are quite sensitive to the weld metal cooling conditions and the weld metal compositions. To describe the cooling rate in the weld metal, the equation given by Ion *et al.* [8] was used. However, concurrent work at ORNL and Pennsylvania State University showed that the cooling rates calculated by the above equation are lower than those expected from computer-aided numerical calculations [9]. These numerical calculations showed that the fluid flow effects in the weld pool enhance the

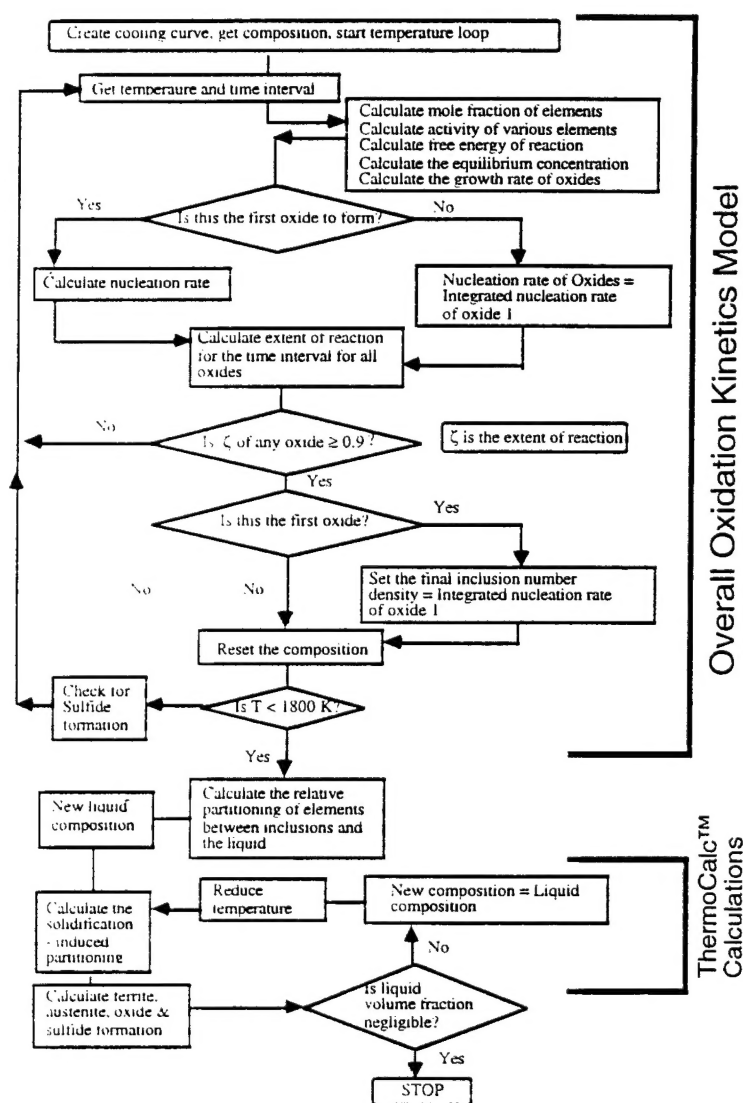


Fig. 2. Overall flow chart of the inclusion model.

thermal conductivity of the liquid pool. Therefore, in this work, enhanced thermal conductivity values were used in cooling rate expressions.

## 2.2. Inclusion Formation during Solidification

During low-alloy steel solidification, alloying elements partition between liquid and solid. As a result of the partitioning, the liquid gets enriched progressively with elements that have a low solubility in the solid as the solidification continues. This enrichment of the liquid results in a higher supersaturation sufficient to initiate some reaction that would not otherwise occur. In the present work, a published model to calculate inclusion formation during stainless steel solidification [5] was applied to the low-alloy steel welds. In this model, complete mixing in liquid and some amount of diffusion in solid are assumed, and the volume fraction of liquid and solid is given by equilibrium calculations. The diffusion in solid was considered using a modified Clyne and Kurz equation [4]. However, the partition coefficient of each element is calculated in an iterative manner at each temperature interval using ThermoCalc™ software [7]. This calculation allows for the consideration of the partition coefficient in a multi-component system, instead of using the partition coefficients from binary alloy systems. The steps are explained in Fig. 2. The governing equations are given below:

$$\Delta C_{\text{liquid}, C-K} = \frac{(1 - f_s)}{\{(1 - f_s) + 2\Omega f_s k\}} \Delta C_{\text{liquid}, \Delta \text{Temp}}, \quad (1)$$

where  $\Delta C_{\text{liquid}, C-K}$  is the effective change in liquid composition after considering the solute diffusion in solid with a change in temperature.  $\Delta C_{\text{liquid}, \Delta \text{Temp}}$  is the calculated equilibrium change in liquid composition without considering the solute diffusion in the liquid,  $f_s$  is the volume fraction of solid,  $k$  is the partitioning coefficient of a corresponding element at a particular temperature, and  $\Omega$  is given by:

$$\Omega = \alpha \left[ 1 - \exp\left(-\frac{1}{\alpha}\right) - 0.5 \exp\left(-\frac{1}{2\alpha}\right) \right] \quad (2)$$

and

$$\alpha = \frac{4Dt}{L^2}, \quad (3)$$

where  $D$  is the diffusivity of a particular element,  $t_i$  is the local solidification time, and  $L$  is the interdendritic spacing.

### 3. Calculation of Continuous Cooling Transformation

In addition to inclusion characteristics, the weld metal hardenability (the driving force for austenite to ferrite transformation) also affects the microstructural development in low-alloy steel welds. To understand and delineate the effects of inclusions and of the hardenability, continuous cooling transformation (CCT) start temperatures for the experimental welds were calculated for a range of cooling rates. There are many published methods to predict the time-temperature-transformation (TTT) diagrams and derive CCT information from the same [10]. In this work, the method developed by Bhadeshia [11] was used. In this method, the time for initiation of transformation is calculated from the following equation:

$$\tau = T^a (\Delta G_{\max}^v)^b \exp\left\{\frac{c}{T}\right\} d \quad (4)$$

where  $\Delta G_{\max}^v$  is the chemical free energy for nucleation of ferrite,  $T$  is the temperature in Kelvin, and  $a$ ,  $b$ ,  $c$ , and  $d$  are constants. This expression is based on the equation suggested by Russell [12] and the values of  $a$ ,  $b$ ,  $c$  and  $d$  are given in ref. 11 for low-alloy steel. (For more detail on the method, see ref. 11). The calculated TTT diagrams are then used to derive the CCT diagram using the additivity rule as given by the following equation:

$$\sum_{i=1}^{i=n} \frac{\Delta t}{\tau_i} = 1 \quad (5)$$

where  $\Delta t$  is the time increment spent at each temperature,  $T_i$ , over the whole cooling rate and  $\tau_i$  is the incubation time for initiation of transformation at  $T_i$ . The temperature at which Eq. (5) is satisfied, is taken as the transformation temperature,  $T_v$ .

### 4. Experimentation

Three experimental welds designed and produced by CSM and Lincoln Electric Company were investigated. The compositions of the welds are given in Table 1. The welding process parameters are tabulated in Table 2. All weld metal specimens were produced by multipass

shielded metal arc welding. The properties of these welds were characterized at CSM and are highlighted in the introduction section of this report. At ORNL, these three welds were characterized with optical microscopy and transmission electron microscopy.

Table 1. Experimental weld metal compositions (wt. %) used in the investigation

No	C	Si	Mn	Ni	Mo	Cr	V	Ti	Cu	N	O
JR1267	0.053	0.29	0.96	2.05	0.48	0.03	0.009	0.033	0.03	0.012	0.030
JR1243	0.057	0.33	1.06	2.53	0.50	0.03	0.006	0.033	0.03	0.019	0.030
JR1273	0.066	0.39	0.98	3.08	0.51	0.03	0.012	0.039	0.03	0.011	0.035

Table 2. Welding conditions used for the production of experimental welds

Shielded Metal Arc Welding Process	
Welding Voltage	22.5 V
Welding Current	170 A
Welding Heat Input	1.0 kJ/mm
Preheat Temperature	298 K
Interpass Temperature	298 - 323 K

After mechanical polishing, the inclusion distributions were measured by optical microscopy in the unetched condition. The inclusion size distributions were measured from the optical micrographs by image analysis on a Macintosh Centris 650 computer using the public domain NIH Image Program [13].

The measured inclusion distribution in optical microscopy represents the 2-D distribution. This 2-D distribution was converted into 3-D distribution using the stereological relations given in ref. 14. The relations are

$$d_v = \frac{\pi}{2} d_u \quad (6)$$

and

$$N_v = \frac{N_u}{d_v} \quad (7)$$

where  $d_v$  is the 3-D inclusion diameter,  $d_u$  is the measured 2-D inclusion diameter,  $N_v$  is the 3-D number density and  $N_u$  is the 2-D number density.

Transmission electron microscopy was also used for measuring inclusion distribution in some cases. The inclusions were extracted from the samples using the carbon extraction replica technique. The extracted replicas mounted on either copper or nylon grids were examined in a Philips-CM12 transmission electron microscope equipped with an energy dispersive X-ray (EDX) analysis system. From transmission electron micrographs, the inclusion sizes were measured

manually. The EDX detector was equipped with an ultrathin window capable of detecting light elements. The inclusion sizes measured in transmission electron micrographs are equivalent to a 3-D diameter. However, to obtain the number density, the number of inclusions has to be divided by the volume analyzed. In this case, the depth of the replica film was taken to be 0.2  $\mu\text{m}$ . The volume was obtained by multiplying the area of analysis by the depth value.

## 5. Results

### 5.1 Inclusion Characteristics

Typical inclusion distributions in the weld JR1273 observed by optical microscopy and transmission electron microscopy are shown in Fig. 3. Both coarse and small inclusions were observed. The measured inclusion size distributions are compared in Fig. 4. The results from optical microscopy showed a peak for the inclusion size  $\sim 0.1 \mu\text{m}$ . This is because of the limitation of the resolution of the optical microscope. The measured inclusion sizes in the optical microscopy are converted into mean 3-D diameter ( $d_v$ ) and 3-D number density ( $N_v$ ) using Eqs. (6) and (7). The arithmetic mean values of all the measurements are compared in Table 3. The measured values from the optical microscopy agree with values from transmission electron microscopy within the

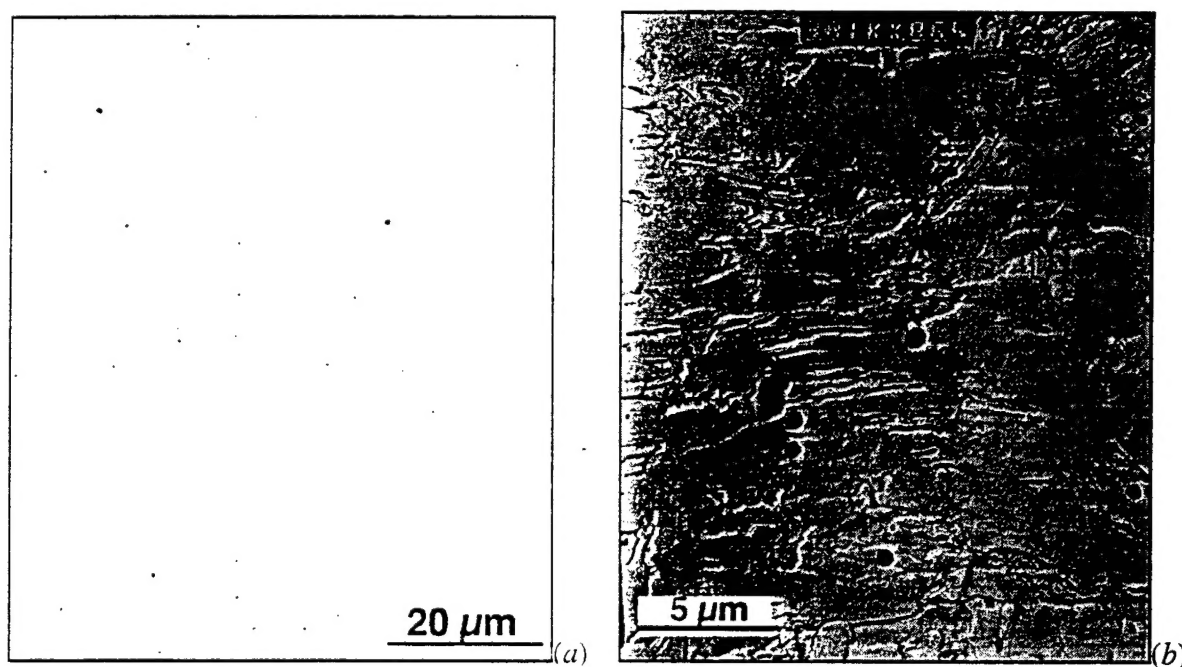


Fig. 3. Typical inclusion distribution in the weld JR1273 observed in (a) optical microscopy and (b) in extraction replica foils with transmission electron microscopy.

experimental errors. The measurements from transmission electron microscopy usually have large errors that are due to the small volume of analysis. The overall results showed only small



differences between the welds. The next stage was to compare the inclusion compositions in the welds.

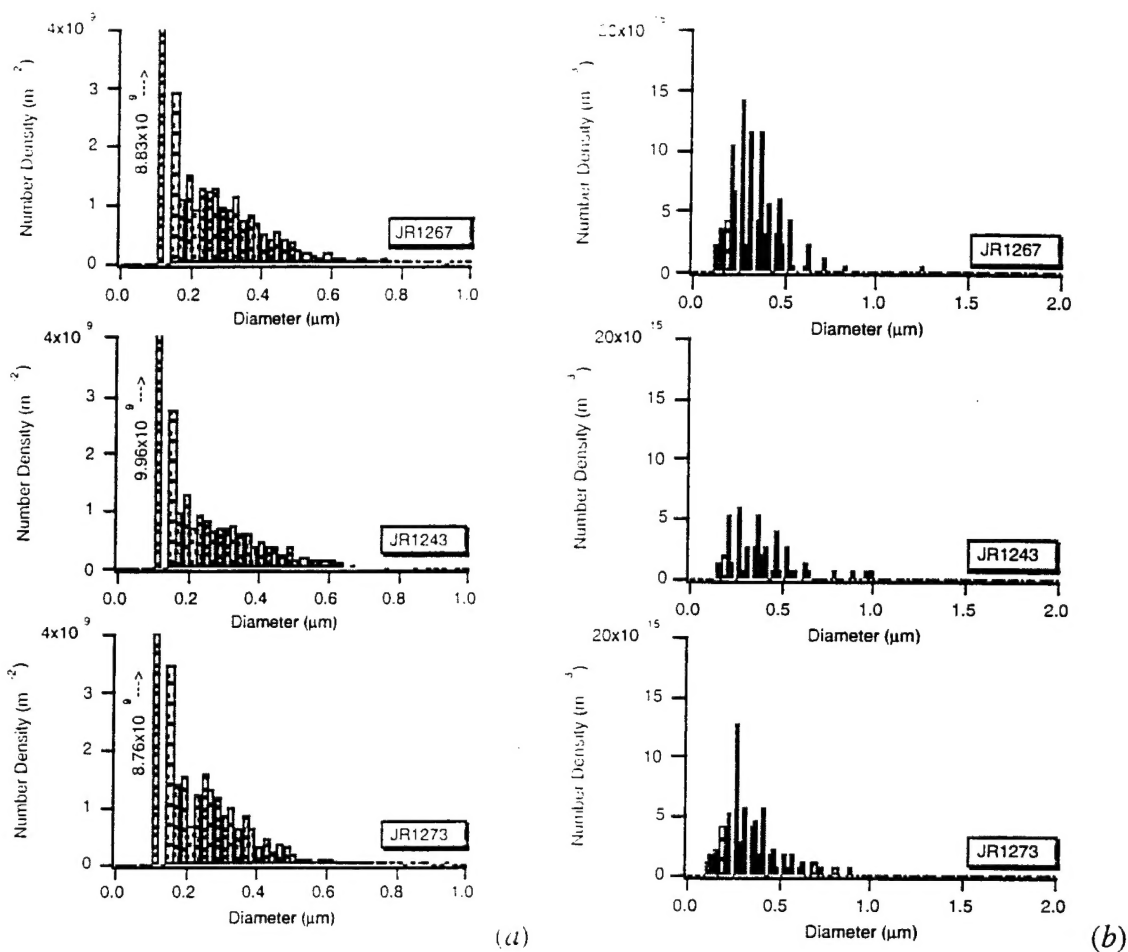


Fig. 4. Comparison of measured inclusion distribution for all the welds (a) measured from optical microscopy and (b) from extraction replica technique.

Table 3. Comparison of overall inclusion size distribution results.

Weld ID	Optical microscopy		Transmission electron microscopy <sup>†</sup>	
	$N_V, m^{-3}$	$d_V, \mu m$	$N_V, m^{-3}$	$d_V, \mu m$
JR1267	7.369e16	0.3892	10.20e17	0.3415
JR1243	7.221e16	0.3452	4.496e16	0.3861
JR1273	7.927e16	0.3528	6.669e16	0.3414

<sup>†</sup> Assumed thickness of replica = 0.2  $\mu m$

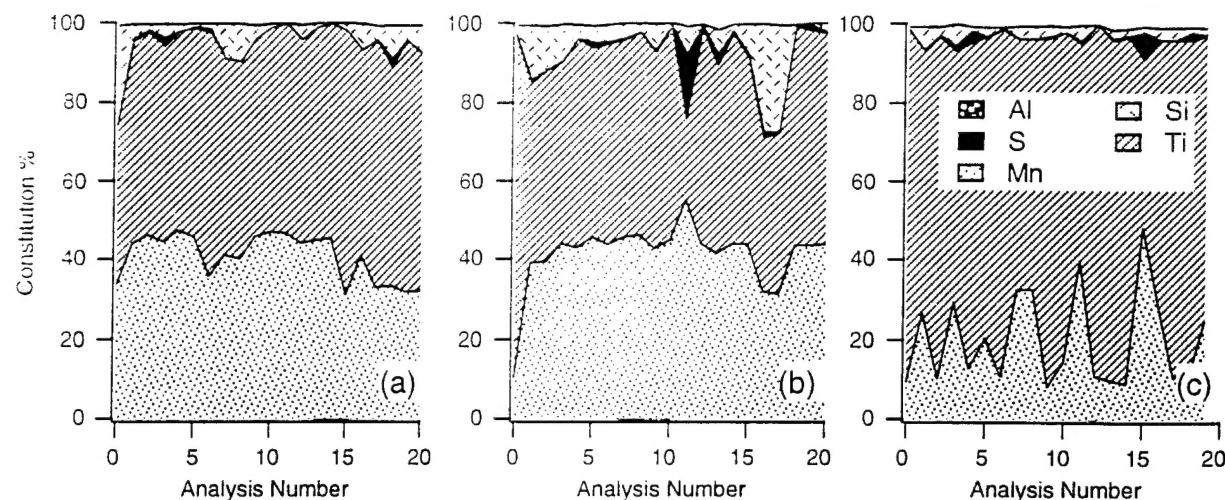


Fig. 5. Summary of EDX analysis on inclusions from all the welds: (a) JR1267, (b) JR1243, and (c) JR1273.

The inclusions in the extraction replica foils were analyzed with EDX. The electron beam spot size was chosen as a way to obtain a compositional analysis from the whole inclusion. However, it is noteworthy that the surface compounds on the inclusion will contribute more to the EDX analysis than will the bulk of the inclusion because of absorption effects. The measured EDX line intensities were converted to elemental concentrations of aluminum, silicon, sulfur, titanium, and manganese using a computer program [15]. Although the oxygen line intensities were measured, they were not considered in the calculation because of uncertainties in the conversion factors. The compositional variations in the welds are compared in Fig. 5. During the analysis, only a few inclusions showed sulfur enrichment indicating the presence of MnS. The plots also indicate that the welds contain titanium rich oxides.

The average composition of inclusions is tabulated in Table 4. Surprisingly, the compositional analysis showed substantially high levels of manganese in almost all the inclusions. The relative manganese to titanium ratio was found to decrease in JR1273 welds compared with JR1267 and JR1243 welds. Since the welds contained negligible amounts of aluminum, the inclusion composition also contained negligible levels of aluminum. In summary, among all the inclusion characteristics, the major difference was found to be in the lower ratio of manganese to titanium concentrations in inclusions in the JR1273 weld compared with JR1267 and JR1243 welds.

Table 4. Comparison of overall composition of inclusions from all the welds

Weld ID	Al	Si	S	Ti	Mn
JR1267	$0.46 \pm 0.06$	$4.56 \pm 1.19$	$0.33 \pm 0.14$	$54.10 \pm 1.31$	$40.54 \pm 1.29$
JR1243	$0.64 \pm 0.22$	$6.58 \pm 1.60$	$2.93 \pm 1.67$	$49.22 \pm 2.58$	$40.63 \pm 1.87$
JR1273	$0.79 \pm 0.08$	$2.33 \pm 0.34$	$0.77 \pm 0.35$	$76.00 \pm 2.98$	$20.12 \pm 2.68$

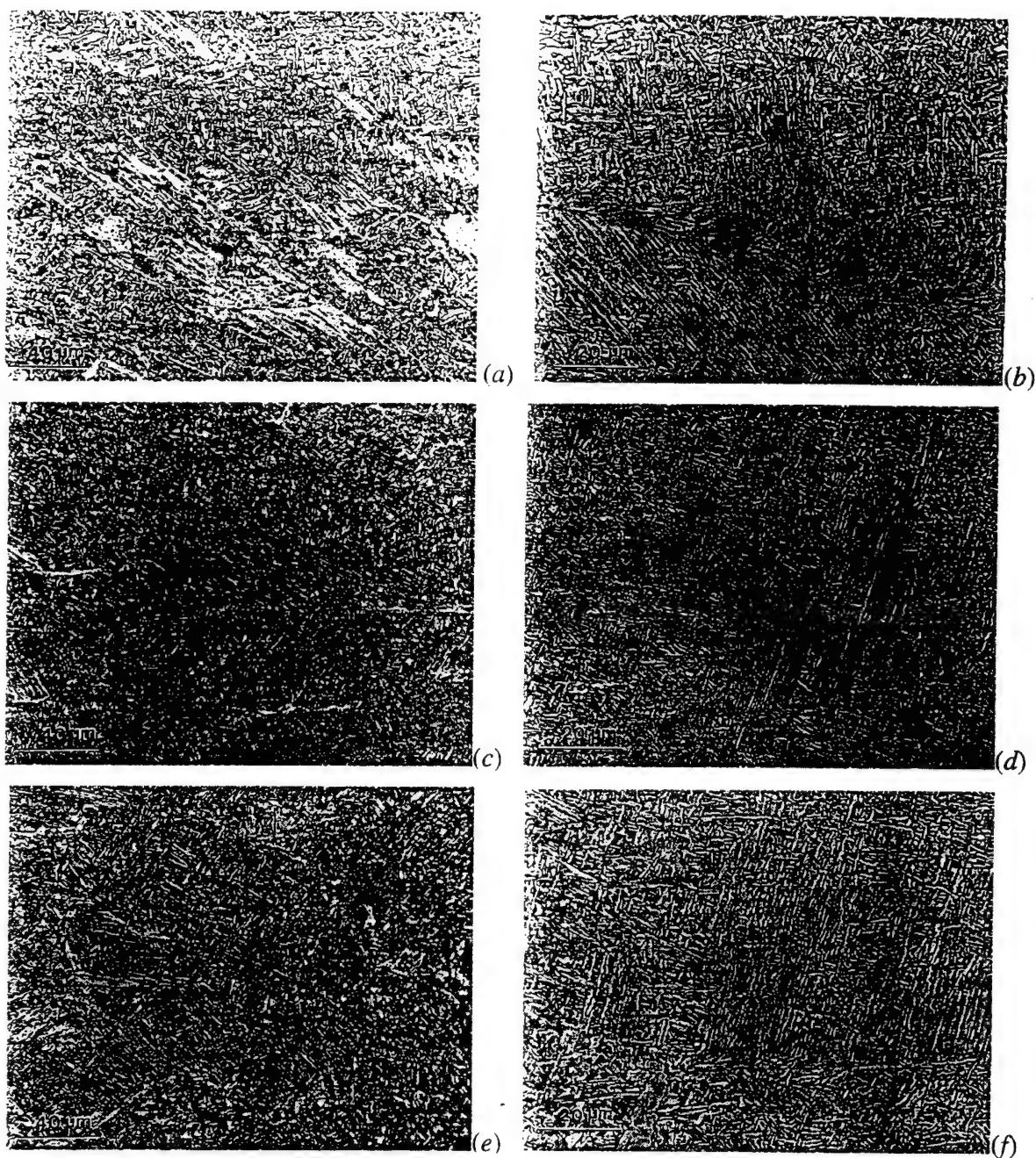


Fig. 6. Low and high magnification optical microstructures of as-welded region of welds: (a) JR1267 (500X); (b) JR1267 (1000X); (c) JR1243 (500X); (d) JR1243 (1000X); (e) JR1273 (500X) and (f) JR1273 (1000X).

## 5.2 Microstructural Development

Optical microscopy of the welds showed the presence of allotriomorphic ferrite, Widmanstätten ferrite, acicular ferrite, bainite, and martensite. However, the volume fractions of allotriomorphic and Widmanstätten ferrite were negligible in JR1243 and JR1273 welds. These

welds have higher nickel concentrations than JR1267. In contrast, the bainitic microstructures were observed in all the welds. The sheaf-like ferrite morphology can be seen in all the microstructures [see Fig. 8(b), (d), and (f)]. Moreover, the microstructures were progressively finer in size with an increase in the nickel concentration. The optical microscopy also indicated both coarse and fine bainitic microstructures co-existing with acicular ferrite. For example, a coarse bainitic sheaf separating two finer acicular ferrite colonies can be seen in Fig. 7. The bainitic sheaf was found to be made up of ferrite sub-units that are in the same orientation in space. The electron diffraction analysis also indicated that the acicular ferrite plates at the bottom and top of the coarse bainitic sheaf have different orientations in space. Further crystallographic analysis may reveal the relative orientation relationship between coarse and fine bainitic ferrite plates and may indicate the mechanism of their transformation from austenite [16].



Fig. 7. Transmission electron micrograph of the bainitic microstructure in weld JR1243. The coarse bainitic sheaf is in  $[001]_{\alpha}$  zone axis. The acicular ferrite colony at the bottom is in  $[\bar{1}11]_{\alpha}$  zone and the top colony is in  $[\bar{1}13]_{\alpha}$  zone axis.

### 5.3 Evaluation of the Inclusion Model

The inclusion model was applied to the three welds. The results after the liquid stage oxidation calculations (up to 1800 K) are presented in Table 5. The calculations clearly indicate oxidation of manganese does not occur above 1800 K. However, the calculations showed the formation of  $Ti_3O_5$  during weld cooling. The overall number density of inclusions was controlled by the  $Ti_3O_5$  formation. The estimates of number density and inclusion diameter compare well with the experimental data. The calculated results did not show drastic differences in the number density of inclusions. This observation is in agreement with experimental results.

Table 5. Results after the liquid stage calculations

Weld	$N_V, m^{-3}$	$d_V, \mu m$	Volume fraction	Al	Ti	Si	Mn
JR1267	9.07e16	0.303	0.00132	—	87	13	—
JR1243	7.06e16	0.331	0.00134	—	85	15	—
JR1273	9.802e16	0.311	0.00154	—	87	13	—

The calculations up to 1800 K showed that there were no sulfide or nitride reactions and showed the presence of residual oxygen (see Table 6). Therefore, the oxide, sulfide, and nitride reactions during solidification were simulated with the procedure outlined in the previous section. The variation of liquid, ferrite, and austenite fractions for three welds is shown in Fig. 8. The solidification temperature, austenite formation temperature, and final fraction were found to change with the increase in nickel levels.

Table 6. Residual composition (wt. %) of liquid steel after the liquid stage calculations.

No	Si	Mn	Ti	S	N	O
JR1267	0.29	0.96	7.7e-4	0.007	0.012	6.7e-3
JR1243	0.32	1.06	11.3e-4	0.007	0.019	6.0e-3
JR1273	0.38	0.98	8.9e-4	0.007	0.011	7.6e-3

The solidification simulation indicated that the residual oxygen<sup>†</sup> will induce one of two reactions: (1) it may combine with residual manganese and silicon and may form  $MnO.SiO_2$  or (2) it may combine with the residual titanium and manganese and may form  $MnO.TiO_2$ . However, the calculations showed that the formation of  $MnO.SiO_2$  was more likely than formation of  $MnO.TiO_2$ . After detailed analysis, it was found that the  $MnO.TiO_2$  cannot form without the suppression of

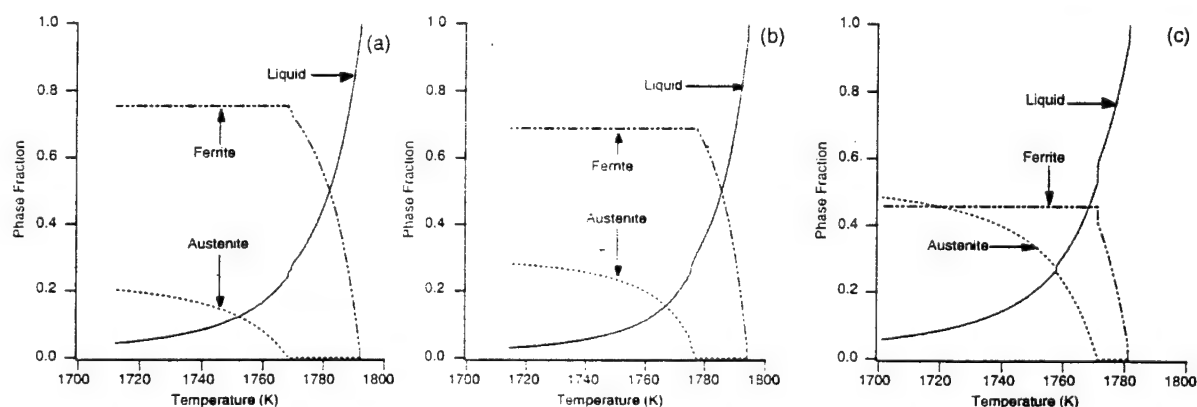


Fig. 8. The comparison of solidification simulations for all three welds: (a) JR1267; (b) JR1243; and (c) JR1273.

<sup>†</sup> This residual oxygen is the amount of oxygen left in the liquid steel just before the solidification. This residual oxygen level is lower than the bulk oxygen levels, because some amount of oxygen would have reacted with deoxidizing elements at high temperatures. The amount of residual oxygen is estimated by the overall oxidation kinetics models outlined in Fig. 2.

MnO.SiO<sub>2</sub> formation. Since the experimental silicon concentration in inclusions was small, the formation of MnO.SiO<sub>2</sub> was intentionally suppressed. The implications of this assumption are discussed in the next section. The effects of solidification simulation on the overall inclusion characteristics are tabulated in Table 7. Overall comparisons of the predicted inclusion characteristics in Tables 5 and 7 with the experimental measurements are shown in Fig. 9. Since the calculations did not predict the formation of sulfides, the inclusion compositions are normalized with reference to titanium, silicon, and manganese.

Table 7. Results after the solidification stage calculations

Weld	Volume fraction	Al	Ti	Si	Mn
JR1267	0.00149	—	77.37	11.46	11.17
JR1243	0.00154	—	74.93	13.05	12.02
JR1273	0.00170	—	81.29	11.79	6.92

The plots in Fig. 9 show that the estimates of inclusion number density, size, and volume fraction compare well with the experimental measurements. The number density and inclusion diameter predictions were notably good. Although the inclusion model predicted that the titanium concentration of inclusions would increase as titanium concentration in the weld increased, the absolute values did not match with the calculations. The experimental concentrations of manganese are higher than the calculated values. Moreover, the calculations did not predict the formation of sulfides or nitrides in all the welds. However, the experimental measurements showed small amounts of sulfide formation, and EDX spectra suggested the presence of small amounts of nitrides on the oxide inclusions. The reasons for this anomaly are discussed in a later section.

## 6. Discussion

The present work has successfully developed a model to describe inclusion formation. The inclusion model considers the oxidation reactions in the temperature range 2300 to 1800 K and considers sulfide and complex oxide formation during solidification as a function of weld metal composition and cooling conditions. In this model, the number density of inclusions was determined by the integrated nucleation rate of the first forming oxide. The model assumed that the first forming oxide would act as a heterogeneous nucleation site for other oxides. Moreover, because of lack of surface energy data at very high temperatures, complete wetting of the first forming oxide was assumed. The model also simulated the solidification effects with a modified Clyne-Kurz equation [4,5] that considers diffusion in the solidifying  $\delta$  ferrite and austenite. The solidification simulation assumed complete mixing in the liquid and described the oxidation reaction in the residual liquid steel as a function of cooling and the fraction of solid formed.

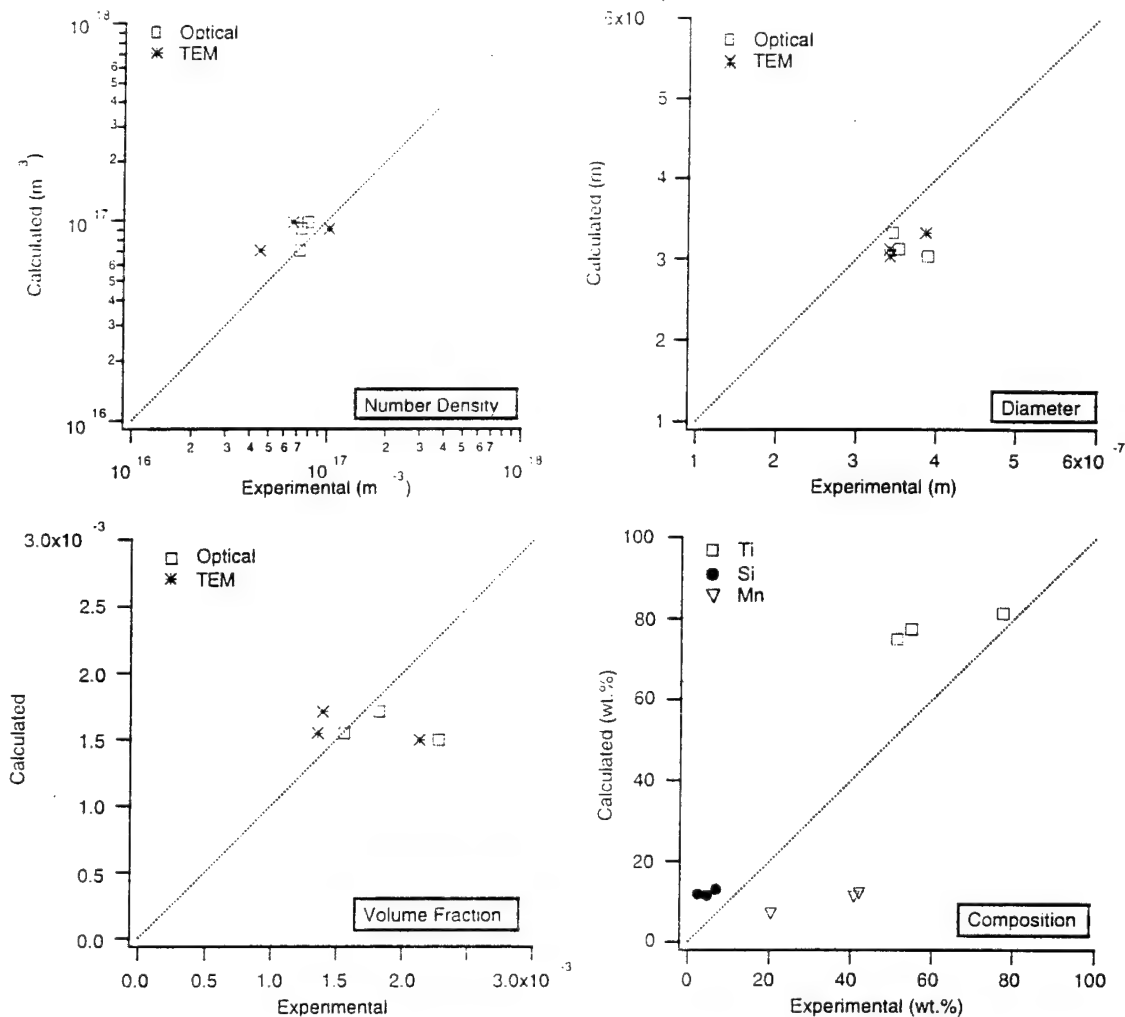


Fig. 9 Comparison of experimental measurements from both optical microscopy and transmission electron microscopy with the inclusion model calculations.

The model was evaluated with three experimental welds. The inclusion model predicted the first forming oxide to be  $Ti_3O_5$  in all three welds. The predicted inclusion number density, size and volume fraction compared well with the experimental data. This result illustrates the validity of the inclusion model. The experimental measurements from both optical and transmission electron microscopy correlated well with the estimated values. The model also indicated that the inclusions in all three welds were titanium rich, which is consistent with the experimental EDX measurements. These results supported the validity of the inclusion model.

Although the model described the complex oxide formation during solidification, the estimates of the inclusion composition did not match with the experimental data. The predicted manganese concentrations in the inclusion were always lower than the experimental measurements. This discrepancy is attributed to the following reasons.



It is expected that, during EDX analysis of inclusions, the surface compounds will contribute more to the EDX spectra than will the core of the inclusions. Therefore, the experimental EDX measurements will correlate well with the last forming compounds. The manganese contribution to the EDX spectra will be higher if the surface compounds were either  $\text{MnO}$ ,  $\text{MnO.SiO}_2$ , or  $\text{MnO.TiO}_2$ .

The inclusion model indicated no oxidation of manganese until it reaches the solidification temperature. This result necessitates further analysis of solidification simulation to explain the observed anomaly. The solidification simulation indicates that  $\text{MnO.TiO}_2$  forms in welds, provided the  $\text{MnO.SiO}_2$  reaction is suppressed. If the  $\text{MnO.SiO}_2$  reaction is not suppressed, the simulations do not yield  $\text{MnO.TiO}_2$ ; and they lead exclusively to  $\text{MnO.SiO}_2$  formation and therefore higher silicon concentration in the inclusions. As a result, for the model to be consistent with the experimental measurements, the  $\text{MnO.SiO}_2$  reaction needs to be suppressed. The reason needs explanation.

The modified Clyne-Kurz model assumes complete mixing in the liquid and assumes the oxidation occurs throughout the residual liquid. However, this may not be the true case. The solidification may induce a heterogeneous composition near the solid-liquid interface compared with liquid far from the interface. For example, near the advancing  $\delta$  ferrite/liquid boundary there will be greater enrichment of manganese than silicon. This variation may induce a different set of oxide reactions (*i.e.*, formation of  $\text{MnO.TiO}_2$  instead of  $\text{MnO.SiO}_2$ ) on the pre-existing inclusions near the solid-liquid interface.

Moreover, this heterogeneous compositional distribution may induce a larger fraction of  $\text{MnO.TiO}_2$  than the one predicted by the present simulation. Such an increase in  $\text{MnO.TiO}_2$  fraction may explain the underestimation of manganese concentration in the inclusions. Further refinement of the inclusion model is necessary considering diffusion within the liquid and [17] considering multi-component diffusion within the solid.

Preliminary work [18] considering multi-component diffusion has successfully described the sulfide reactions during solidification in a multi-component steel. However, the description of sulfide and oxide reaction with diffusion in solid and liquid was found to be complex and is beyond the scope of the present work. Thermodynamic calculations also indicated that the nitride reaction will be initiated only in the solid state, that is, in the austenite phase during weld cooling.

In summary, the inclusion model and the experimental data have shown that there are only minor differences in the inclusion characteristics among three welds JR1267, JR1243, and JR1273, except for the Mn to Ti ratio of inclusion composition in the JR1273 weld. However, JR1273 and JR1243 welds exhibit similar microstructure and toughness in spite of different inclusion composition. Therefore, it is concluded that the observed differences in toughness and microstructure in welds should be attributed to a change in the  $\gamma$  to  $\alpha$  transformation characteristics.



With an increase in the nickel concentrations in the weld, the as-welded microstructure became finer. In JR1267 welds (2.05 wt. % Ni), both allotriomorphic and Widmanstätten ferrite [see Fig. 8(b)] were observed, in addition to acicular ferrite and bainite [see Fig. 8(a)]. In comparison, the JR1243 (2.53 wt. % Ni) and JR1273 (3.08 wt. % Ni) welds showed negligible amounts of allotriomorphic ferrite and Widmanstätten ferrite. Moreover, JR1243 and JR1273 welds showed mixtures of bainite and acicular ferrite. For example, the transmission electron microscopy revealed the presence of coarse bainitic sheaves separating finer acicular ferrite colonies in JR1243 welds (see Fig. 7). The differences in size of the sheaves compared with ferrite plates in the colony suggest that this coarse bainite might have formed at high temperatures than those of the other plates. As a result, the acicular ferrite colony on either side formed with different spatial orientations. All the welds revealed some amount of martensitic islands in the as-welded region. The absence of ferrite phases such as allotriomorphic and Widmanstätten ferrites may be attributed to the toughness improvement in JR1243 and JR1273 welds, in addition to refinement of the microstructure.

An increase in nickel concentration will lead to a change in  $\gamma$  to  $\alpha$  transformation characteristics. This change can be illustrated with CCT curves. The CCT curves for the initiation of transformation were calculated for three welds using the method outlined before (Fig. 11). The plots indicate that the transformation kinetics of austenite will be retarded because of the addition of nickel. Therefore, for a given cooling rate, JR1243 and JR1273 welds will transform at lower temperatures, leading to a higher fraction of low-temperature ferrite morphologies such as bainite,

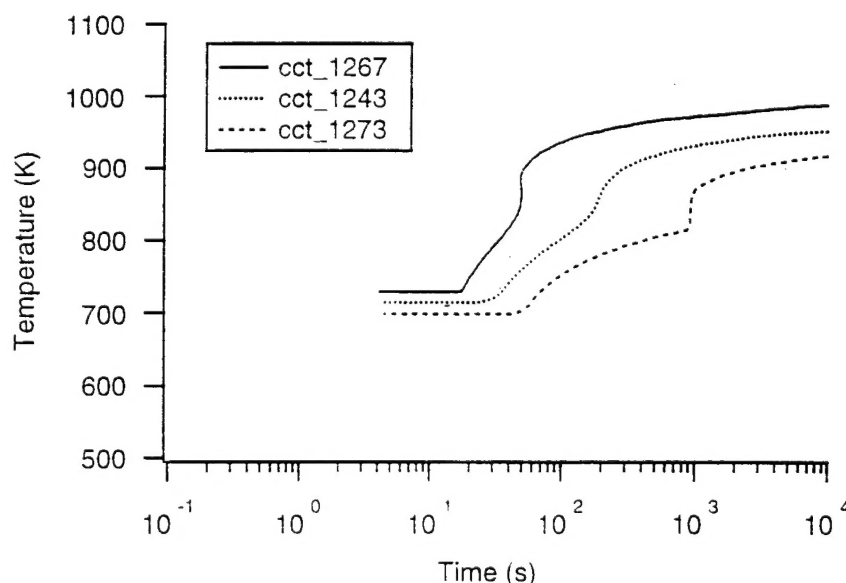


Fig. 11 Calculated CCT transformation initiation diagrams for three welds JR1267, JR1243, and JR1273.

acicular ferrite, and martensite. The calculations are consistent with the observed microstructure. Using these calculated data, it is possible to estimate the fractions of various phases theoretically [19]. However, this is beyond the scope of the present work. In summary, the present work shows the inclusion characteristics in all the welds are capable of initiating the acicular ferrite transformation, since they are indeed made up of titanium-rich oxides [20]. Therefore, in the present welds, the relative fractions of various phases depend more predominantly on the hardenability of the welds than on the inclusion characteristics.

## 7. Summary

A two-stage inclusion model capable of describing the oxidation reaction above and below the solidification start temperature has been developed. This model can describe the inclusion formation as a function of weld metal composition and cooling rate and estimate the inclusion number density, size, volume fraction, and composition and the concentration of residual deoxidizer element concentrations. The inclusion characteristics from three welds with differing nickel concentrations were measured using optical and transmission electron microscopy. The model predictions of inclusion number density, size and volume fraction compare well with the experimental measurements. The inclusion model also predicted the trends of inclusion composition; however, the values did not match accurately. The observed discrepancy is attributed to the limitations of the solidification simulation method to describe the heterogeneous compositional distribution ahead of the solid/liquid interface.

The microstructure of welds became progressively finer with an increase in nickel concentration. The allotriomorphic and Widmanstätten ferrite volume fractions were negligible in high-nickel welds. In all the welds, the microstructure was predominantly a mixture of acicular ferrite and bainite with small amounts of martensitic islands. In all the welds, coarse bainitic sheaves were observed in islands of small acicular ferrite or bainite plates. The microstructural development in all the welds correlates well with a calculated CCT diagram. The observed variation in toughness is attributed to a change in microstructural development induced by a change in nickel concentrations.

## 8. Reference

- [1] S. S. Babu, S. A. David, and G. R. Edwards: "High-Strength Steel Welding Research," Report No. 1, 1995.
- [2] S. A. David and S. S. Babu: "Microstructure modeling in weld metal," *Proc. International Conference on Numerical Analysis of Weldability*, Graz-Saggau, Austria, September 25-27, 1995.

- [3] S. S. Babu, J. M. Vitek, S. A. David, K. Mundra, and T. DebRoy: "Model for inclusion formation in low alloy steel welds." 77<sup>th</sup> American Welding Convention, Chicago, April, 24, 1996.
- [4] T. W. Clyne and W. Kurz: *Metall. Trans. A.*, **12A**, (1981), p. 965.
- [5] T. Matsumiya, T. Koseki, W. Yamada, and Y. Ueshima: *Nippon Steel Technical Report*, **57** (1993), p. 50.
- [6] M. Clark and G. R. Edwards: Unpublished Research, 1996, Colorado School of Mines.
- [7] B. Sundman, B. Jansson, and J. O. Andersson: *Calphad*, **9** (1985), p. 153.
- [8] J. C. Ion, K. E. Easterling, and M. F. Ashby: *Acta Metall.*, **32** (1984), p. 1949.
- [9] S. S. Babu, S. A. David, J. M. Vitek, K. Mundra and T. DebRoy: *Proc. Trends in Welding Research*, Gatlinburg, Tennessee, June 5-8, (1995).
- [10] D. F. Watt, L. Coon, M. Bibby, J. Goldak and C. Henwood: *Acta. Metall.* **36** (1988), p. 3029.
- [11] H. K. D. H. Bhadeshia: *Metal Science*, **16** (1982), p. 159.
- [12] K. C. Russell: *Acta. Metall.* **17** (1969) p. 1123.
- [13] Wayne Rasband, NIH-Image, U.S. National Institute of Health, Springfield, Virginia.
- [14] A. Kluken and Ø. Grong: *Metall. Trans. A.*, **20A** (1989), p. 1335.
- [15] N. Evans and E. Kenick: *Private Communication*, Oak Ridge National Laboratory, 1996.
- [16] S. S. Babu and H. K. D. H. Bhadeshia: *Mater. Sci. and Engg.*, **A142** (1991) p. 209.
- [17] J. O. Andersson, L. Höglund, B. Jönsson, and J. Ågren: *Fundamentals and Applications of Ternary Diffusion*, G. R. Purdy, ed., Pergamon Press, New York, NY, 1990, p. 153.
- [18] S. S. Babu, S. A. David, and J. M. Vitek: *Unpublished Research*, Oak Ridge National Laboratory, Oak Ridge, 1996.
- [19] H. K. D. H. Bhadeshia, L.E. Svensson, and B. Gretoft: *Acta Metall.*, **33** (1985) p. 1271.
- [20] H. K. D. H. Bhadeshia: *Bainite In Steels*, Institute of Materials, London, (1992).